AGU PUBLICATIONS

Journal of Advances in Modeling Earth Systems

RESEARCH ARTICLE

10.1002/2015MS000529

Key Points:
- CRM with three methods of parameterized large-scale dynamics captures rain rates of the DYNAMO MJO events
- Horizontal advection of moisture reduces the precipitation and suppresses the top-heaviness of *W*
- Radiative feedbacks significantly amplify the MJO

Correspondence to:
S. Wang,
sw2526@columbia.edu

Citation:
Wang, S., A. H. Sobel, and J. Nie (2016), Modeling the MJO in a cloud-resolving model with parameterized large-scale dynamics: Vertical structure, radiation, and horizontal advection of dry air, *J. Adv. Model. Earth Syst.*, *8*, doi:10.1002/2015MS000529.

Received 6 AUG 2015
Accepted 24 DEC 2015
Accepted article online 31 DEC 2015

© 2015. The Authors.
This is an open access article under the terms of the Creative Commons Attribution-NonCommercial-NoDerivs License, which permits use and distribution in any medium, provided the original work is properly cited, the use is non-commercial and no modifications or adaptations are made.

Modeling the MJO in a cloud-resolving model with parameterized large-scale dynamics: Vertical structure, radiation, and horizontal advection of dry air

Shuguang Wang[1], Adam H. Sobel[1,2], and Ji Nie[2]

[1]Department of Applied Physics and Applied Mathematics, Columbia University, New York, New York, USA, [2]Lamont-Doherty Earth Observatory of Columbia University, Palisades, New York, New York, USA

Abstract Two Madden-Julian Oscillation (MJO) events, observed during October and November 2011 in the equatorial Indian Ocean during the DYNAMO field campaign, are simulated in a limited-area cloud-resolving model using parameterized large-scale dynamics. Three parameterizations of large-scale dynamics—the conventional weak temperature gradient (WTG) approximation, vertical mode-based spectral WTG (SWTG), and damped gravity wave coupling (DGW)—are employed. A number of changes to the implementation of the large-scale parameterizations, as well as the model itself, are made and lead to improvements in the results. Simulations using all three methods, with imposed time-dependent radiation and horizontal moisture advection, capture the time variations in precipitation associated with the two MJO events well. The three methods produce significant differences in the large-scale vertical motion profile, however. WTG produces the most top-heavy profile, while DGW's is less so, and SWTG produces a profile between the two, and in better agreement with observations. Numerical experiments without horizontal advection of moisture suggest that that process significantly reduces the precipitation and suppresses the top-heaviness of large-scale vertical motion during the MJO active phases. Experiments in which a temporally constant radiative heating profile is used indicate that radiative feedbacks significantly amplify the MJO. Experiments in which interactive radiation is used produce agreement with observations that is much better than that achieved in previous work, though not as good as that with imposed time-varying radiative heating. Our results highlight the importance of both horizontal advection of moisture and radiative feedbacks to the dynamics of the MJO.

1. Introduction

The interaction between moist convection and large-scale atmospheric dynamics remains a fundamental scientific problem, one that is important to prediction on a range of time scales, from short-term weather prediction to multidecadal climate projection. Numerical models with horizontal grid spacings on the order of a kilometer, capable of resolving cloud systems without error-prone cumulus parameterization, have become an essential tool for studying moist convection, though they remain (for the moment) impractical for most operational prediction. These models are often known as cloud-resolving models or cloud system-resolving models (CRMs).

For basic research oriented at gaining physical insight into the interaction of moist convection with large-scale dynamics, CRMs coupled to a parameterization of large-scale dynamics offer an attractive strategy. Several such parameterizations have been developed [e.g., *Sobel and Bretherton*, 2000; *Mapes*, 2004; *Bergman and Sardeshmukh*, 2004; *Raymond and Zeng*, 2005; *Kuang*, 2008; *Romps*, 2012a; *Wang and Sobel*, 2011, 2012; *Daleu et al.*, 2012, 2015b; *Herman and Raymond*, 2014; *Nie and Sobel*, 2016], and the approach has matured to the point that an intercomparison has been carried out [*Daleu et al.*, 2015a].

Much research using these methods has involved idealized simulations. Research designed to investigate time-varying weather and climate phenomena has mostly involved "time-slice" simulations run to equilibrium with boundary conditions or forcings that are steady in each run, but taken from different phases of phenomena such as ENSO [*Chiang and Sobel*, 2002], tropical depressions [*Raymond and Sessions*, 2007], multiple equilibria [*Sobel et al.*, 2007; *Sessions et al.*, 2010, 2015], the quasi-biennial oscillation [*Nie and Sobel*, 2015], and seasonal cycles in the Amazon [*Anber et al.*, 2015]. Only recently have attempts been made to

simulate time-varying observations in single simulations with time-dependent forcings. *Wang et al*. [2013] used the weak temperature gradient (WTG) and damped gravity wave (DGW) methods to simulate a sequence of observed MJO events in the Pacific from the TOGA COARE field campaign; and *Edman and Romps* [2015] simulated observed time sequences of both tropical and midlatitude convective events using several large-scale parameterizations. Here we extend this work to the MJO observed in the Indian Ocean during the Cooperative Indian Ocean Experiment on Intraseasonal Variability in Year 2011/Dynamics of the Madden-Julian Oscillation (CINDY/DYNAMO, hereafter DYNAMO) field campaign [*Yoneyama et al*., 2013]. For the same MJO events, *Sentic et al*. [2015] also performed numerical simulations using the SWTG method and found that their simulations were capable of reproducing important relations between convection and large-scale environment—including atmospheric stability, moisture, and gross moist stability.

Here after modifications to both the WRF model itself and the implementation of the large-scale dynamics parameterizations for this purpose, we are able to achieve more accurate results than we would with the methods of *Wang et al*. [2013]. We further perform a set of mechanism denial experiments to determine the importance of physical processes, most specifically horizontal advection and cloud-radiative interaction, to the simulated MJO events. We also compare three different parameterizations of large-scale dynamics, including WTG, DGW, and a "spectral WTG" (SWTG) similar to that introduced by *Herman and Raymond* [2014], but using the vertical modes associated with the observed stable stratification rather than the more idealized sinusoids as a basis.

The rest of the article is structured as follows: section 2 contains descriptions of the observed case under study; the methods used here to parameterize large-scale dynamics and their implementation for the simulation with time-dependent observations; and details of the numerical model. Section 3 contains the main results. Discussion and conclusions are presented in section 4.

2. Case Description and Methods

2.1. Case Description: Observed MJO Events at the NSA During DYNAMO

During October, November and early December 2011, two MJO events were observed in the equatorial Indian Ocean and well sampled by the DYNAMO northern sounding array (NSA) [*Johnson and Ciesielski*, 2013; *Sobel et al*., 2014; *Johnson et al*., 2015]. The NSA was located immediately north of the equator in the central equatorial Indian Ocean. It was defined by four sounding sites: Gan Island, Maldives (0.698°N, 73.518°E), Malé, Maldives (4.918°N, 73.538°E), Colombo, Sri Lanka (6.918°N, 79.878°E), and the R/V Revelle (0.008°N, 80.508°E). Figure 1a shows these two MJO events in time series of surface rain rate from TRMM and net column radiation from CERES SYN1deg daily radiative fluxes (Clouds and the Earth's Radiant Energy System) [*Wielicki et al*., 1996; *Loeb et al*., 2012], both averaged over the NSA. Large-scale vertical motion derived from the NSA (Figure 1b) shows strong ascent peaking at 10–12 km during the active phases, and weak descent in the suppressed phases. An important feature of these MJO events is pronounced horizontal moisture advection, shown in Figure 1c as derived from the NSA sounding data [*Johnson and Ciesielski* 2013; *Ciesielski et al*., 2014]. This figure shows significant drying at the beginning of October and the end of November (day 55-60), when it reaches 3-4 g kg^{-1} d^{-1}. These drying episodes are associated with low-level westerly winds (Figure 1d). The synoptic pattern associated with these westerlies was discussed in detail in *Sobel et al*. [2014]. The time series of daily sea surface temperature (Figure 1e) shows relatively low values (28.7°C) in early October with variations of less than 0.5°C for the most of the period, but increases by 0.5°C during the suppressed phase in the first 2 weeks of November. *Wang et al*. [2015b] found, in regional numerical simulations with WRF on realistic Indian Ocean geography, that including these SST variations was not important to their simulation of the October MJO event, while it was much more significant for the November MJO event.

2.2. Parameterizations of Large-Scale Dynamics

Parameterizations of large-scale dynamics are used for simulations of atmospheric convection in either a single column model or a limited-area doubly periodic CRM. Tendencies representing domain-averaged advection can be important to the thermodynamics, but are coupled to dynamics outside the computational domain. Parameterizations of large-scale dynamics allow these larger-scale dynamics to be represented in idealized but plausible ways, simplifying analysis and allowing computational resources to be focused on the convection itself.

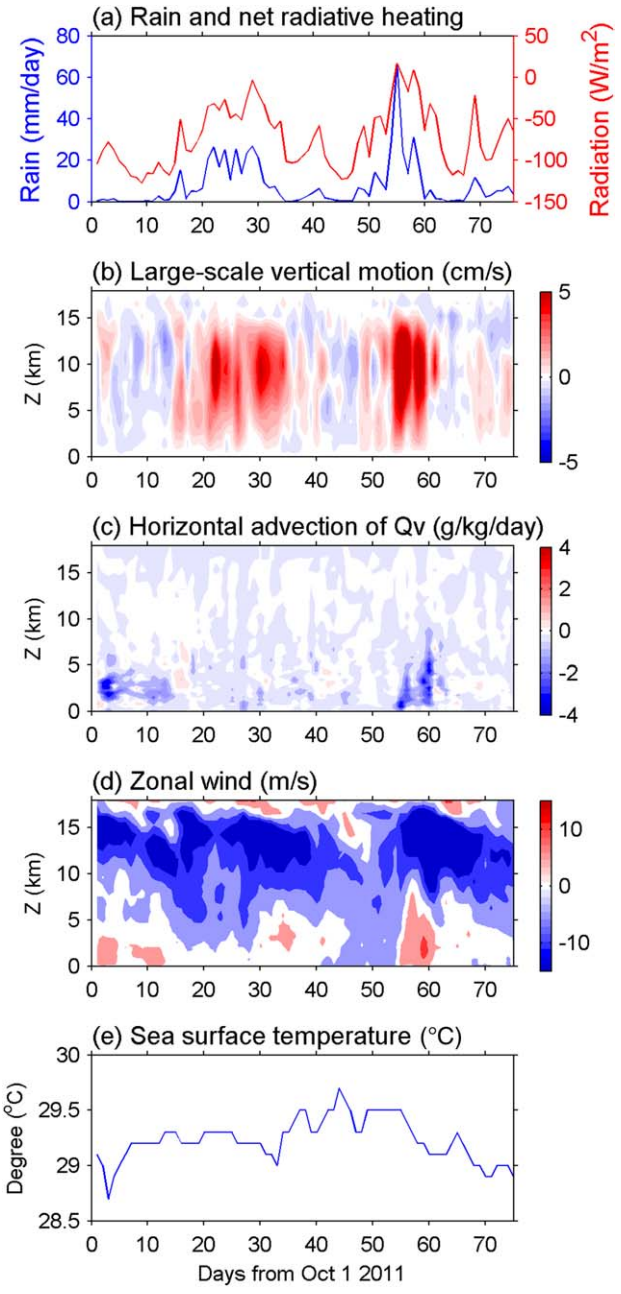

Figure 1. (a) Time series of rain and column-integrated radiative heating from CERES over northern sounding array (NSA), (b) large-scale vertical motion (cm/s) from NSA, (c) horizontal advection of moisture (g/kg/d) from the northern sounding array (NSA), (d) zonal wind from NSA, and (e) daily sea surface temperature (°C).

Our thermodynamic equations can be written, somewhat generically:

$$\frac{\partial \theta}{\partial t} + \cdots = -W\frac{\partial \theta}{\partial z}$$

$$\frac{\partial Q}{\partial t} + \cdots = -W\frac{\partial Q}{\partial z} - Q_{hadv}$$

where θ and Q are potential temperature and water vapor mixing ratio, respectively; W is the large-scale vertical motion; and Q_{hadv} is horizontal advective tendency of moisture ($\vec{V}_h \nabla Q$, where $\vec{V}_h$ is horizontal winds). The horizontal advective tendency of potential temperature is neglected in the first equation due to its small amplitude in the tropics. The other advective tendencies can, if desired, be externally specified [e.g., *Grabowski et al.*, 1996] using observationally derived values. The vertical advective tendencies in particular can be either directly specified, or computed from observed vertical velocity combined with simulated vertical gradients of the thermodynamic variables. Here we use the latter method, implemented similarly to *Wang et al.* [2015a], for our "control" simulation, which we also refer to as the "simulation with imposed large-scale dynamics."

However, specifying the vertical advective tendencies, in particular, arguably misrepresents causality [*Mapes*, 1997, 2004]. In response to this critique, a number of methods have been developed to parameterize the large-scale vertical motion (and vertical advective tendencies) via truncations of large-scale atmospheric dynamics [e.g., *Sobel and Bretherton*, 2000; *Raymond and Zeng*, 2005; *Kuang*, 2008; *Romps*, 2012a, 2012b; *Wang et al.*, 2013; *Herman and Raymond*, 2014; *Edman and Romps*, 2015]. In this study, we will present column simulations of the MJO rain rates using three such methods: conventional WTG, vertical mode-based spectral WTG, (SWTG), and damped gravity wave coupling (DGW). In each method, large-scale vertical motion is derived as part of the model solution (details below), and used for advecting domain-averaged temperature and moisture in the vertical. Brief introductions to WTG and DGW are given below, followed by a more detailed description of our vertical mode-based implementation of spectral WTG.

2.2.1. The Weak Temperature Gradient Method

In the WTG method, large-scale vertical velocity W in the free troposphere at any instant is derived by assuming that large-scale vertical advection acts to restore the virtual potential temperature to a target profile:

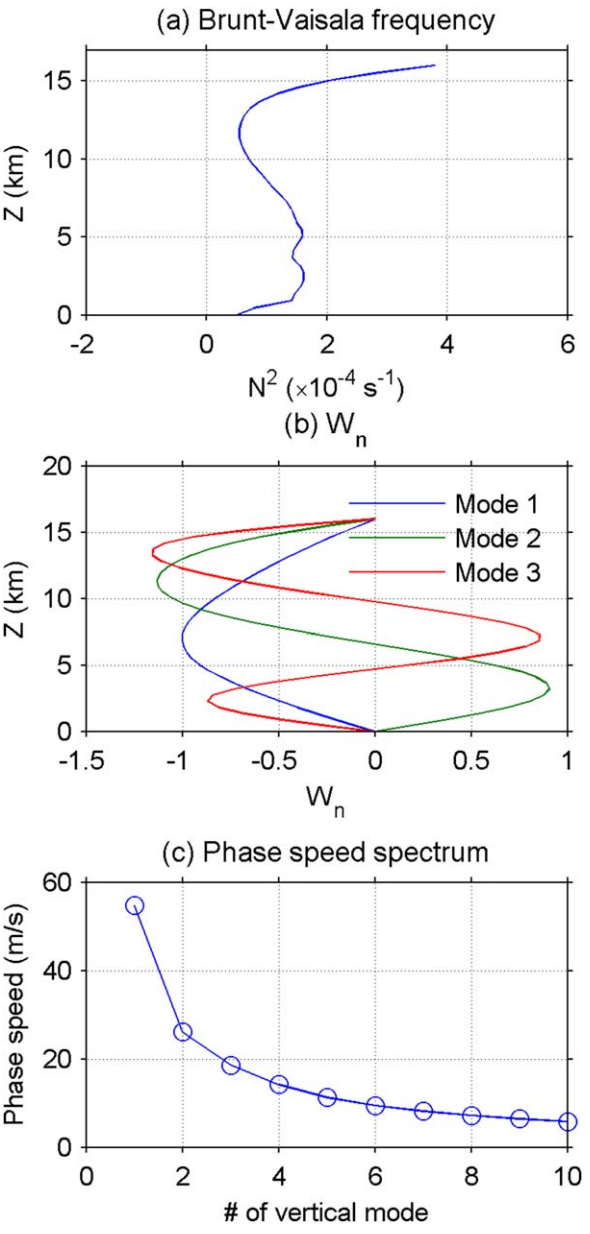

Figure 2. (a) Time-mean Brunt-Väisälä frequency of the DYNAMO Northern Sounding Array. (b) The first three gravity modes of mass fluxes. (c) Phase speeds of the first 10 gravity modes.

$$W\frac{\partial\theta_v}{\partial z}=\frac{\theta_v-\theta_v^B}{\tau}, \tag{1}$$

where θ_v is the virtual potential temperature horizontally averaged over the CRM domain, and θ_v^B is the target virtual potential temperature, a function of time and height, assumed to represent the larger-scale environment in which the region being simulated is embedded. Equation (1) is applied in the free troposphere. In the boundary layer, we linearly interpolate W between its value at the top of boundary layer obtained from equation (1) and its surface value $W=0$. Here the nominal boundary layer height is taken as 1.5 km, so we apply equation (1) from 1.5 to 17 km (∼100 hPa), nominal tropopause height. θ_v^B is the "target" value to which potential temperature is relaxed at a time scale of $\tau=1$ h. We also place a lower bound on the value of $\frac{\partial\theta_v}{\partial z}$, replacing the observed value by 1 K/km if it becomes smaller than that bound, as *Raymond and Zeng* [2005]. Although this occurs very rarely in the free troposphere, it is helpful to prevent unrealistically large values of W.

2.2.2. The Damped Gravity Wave Method

The damped gravity wave method was developed by *Kuang* [2008; see also *Blossey et al*., 2009; *Kuang*, 2011, 2012]. It has also been rationalized from a different perspective by *Romps* [2012a, 2012b], and modified further by *Edman and Romps* [2014, 2015]. In this study, the large-scale vertical velocity is diagnosed from virtual temperature anomalies as in *Blossey et al*. [2009] or *Kuang* [2011]:

$$\frac{\partial}{\partial p}\left(\varepsilon\frac{\partial\omega}{\partial p}\right)=\frac{k^2R_d}{p}(T_v-T_v^B), \tag{2}$$

where p is pressure, ω is pressure velocity, ε is the inverse time scale for Rayleigh momentum damping, k is the wave number, R_d is the dry gas constant, T_v is the domain-averaged virtual temperature, and T_v^B is the target virtual temperature against which linearized wave perturbations are defined. In idealized simulations T_v^B is taken constant in time, while here it is set to the observed time-varying virtual temperature profile. For the experiments below, we choose $\varepsilon=1$ d^{-1} and $k=2\times10^{-6}$ m^{-1}. Equation (2) is solved with boundary conditions $\omega=0$ at the surface and 100 hPa.

2.2.3. Spectral WTG Based on the Vertical Structure Equation

Past studies have demonstrated that a vertical mode transform is useful for understanding the dynamics of stratified fluids [*Gill*, 1980], and tropical atmosphere in particular [*Fulton and Schubert*, 1985; *Wu et al*., 2000; *Bergman and Sardeshmukh*, 2004; *Mapes*, 2004; *Tulich et al*., 2007]. Here we will develop a version of spectral WTG [*Herman and Raymond*, 2014] based on the vertical mode transform. We start from the two-dimensional anelastic equations in the absence of rotation:

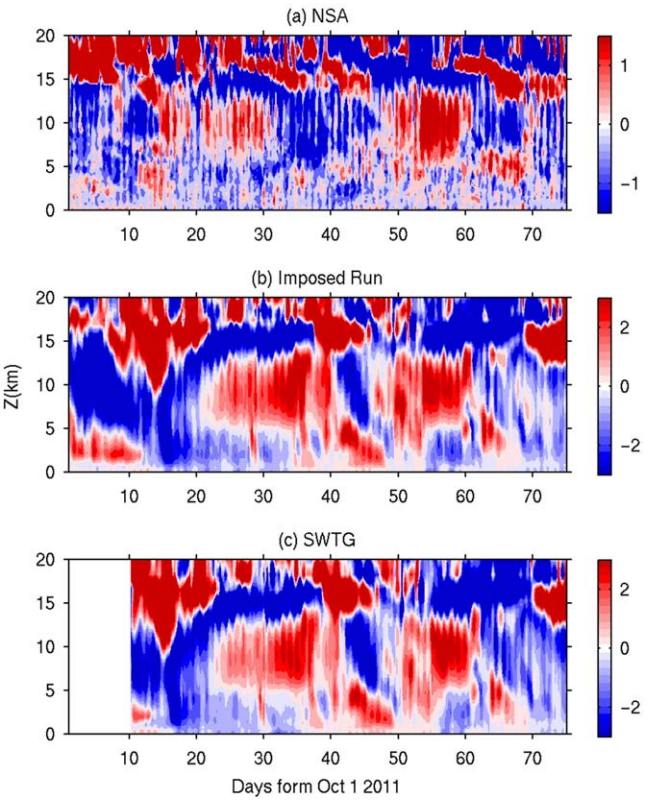

Figure 3. Temperature anomaly from (a) NSA, (b) the imposed run, and (c) the spectral WTG run using temperature anomalies from the imposed run.

$$\begin{aligned} u_t &= -p_x \\ p_z &= b \\ u_x + (\rho_0 w)_z/\rho_0 &= 0 \\ b_t + wN^2 &= 0, \end{aligned} \tag{3}$$

where b is buoyancy, u, v, w, are horizontal and vertical winds, p is pressure, and $N^2(z)$ is the Brunt-Väisälä frequency, $\rho_0(z)$ is a reference density profile; and subscripts indicate partial derivatives. Assume wave solutions in the horizontal, and let $(u, p, w, b) = [U(z), P(z), W(z), B(z)]e^{i(kx-\omega t)}$. Eliminating variables other than $W(z)$ leads to the vertical structure equation:

$$\frac{\partial^2}{\partial z^2}(\rho_0 W) + \frac{1}{c^2}N^2(\rho_0 W) = 0, \tag{4}$$

where c is the phase speed. Rigid boundary conditions may be used:

$$W = 0 \text{ at } z = 0,\ H, \tag{5}$$

where H is the height of the tropopause. The rigid lid at the tropopause is used here for simplicity, though a radiative upper boundary condition would be more accurate. The vertical structure equation (4) and boundary condition (5) constitute a Sturm-Liouville problem, which has an infinite number of real eigenvalues and corresponding eigenfunctions. The eigenfunctions form an orthogonal basis with respect to the inner product defined as:

$$\langle W_m, W_n \rangle = \int_0^H W_m \cdot W_n \cdot N^2 dz = \langle W_n, W_n \rangle \delta_{mn}, \tag{6}$$

where δ_{mn} is the Kronecker delta function. For each mode W_n, the eigenvalue $1/c_n^2$ may be interpreted as the inverse of the horizontal phase speed squared of that mode.

This Sturm-Liouville problem (4) and (5) is solved numerically by discretizing the second order differential operator into a tridiagonal matrix, and then searching for eigenvalues using the Matlab® function *eigs*. A total of 35 equally spaced levels from the surface to the tropopause are used to solve the generalized matrix eigenvalue problem. Based on the time-mean profile of the Brunt-Väisälä frequency (Figure 2a) derived from the NSA observations, the first three modes thus computed are shown in Figure 2b, whose phase speeds c are 55, 26, and 19 m/s (Figure 2c), respectively. The phase speed c decreases approximately as $1/m$, where m is the vertical wave number.

We now describe a spectral WTG method which is similar to that of *Herman and Raymond* [2014], but based on the vertical modes as derived above. We expand $W = \sum v_n W_n$, where v_n is the expansion coefficient. Assuming WTG is approximately respected for each individual mode, the temperature anomaly projected onto each mode is removed by that mode such that $v_n = j_n \tau_n^{-1}$, where j_n is the projection of potential temperature anomaly onto gravity wave mode n,

$$j_n = \left\langle \rho \frac{\overline{\theta_v} - \theta_v^{\beta}}{\partial_z \overline{\theta_v}}, W_n \right\rangle \Big/ \langle W_n, W_n \rangle. \tag{7}$$

We let the time scale τ_n be $\tau_1^{-1} = \tau_1^{-1}\left(\frac{c_n}{c_1}\right)^{\alpha}$ where τ_1 is the time scale of the gravest mode, c_n is the phase speed of mode n, and the exponent α is discussed below. W may be approximated:

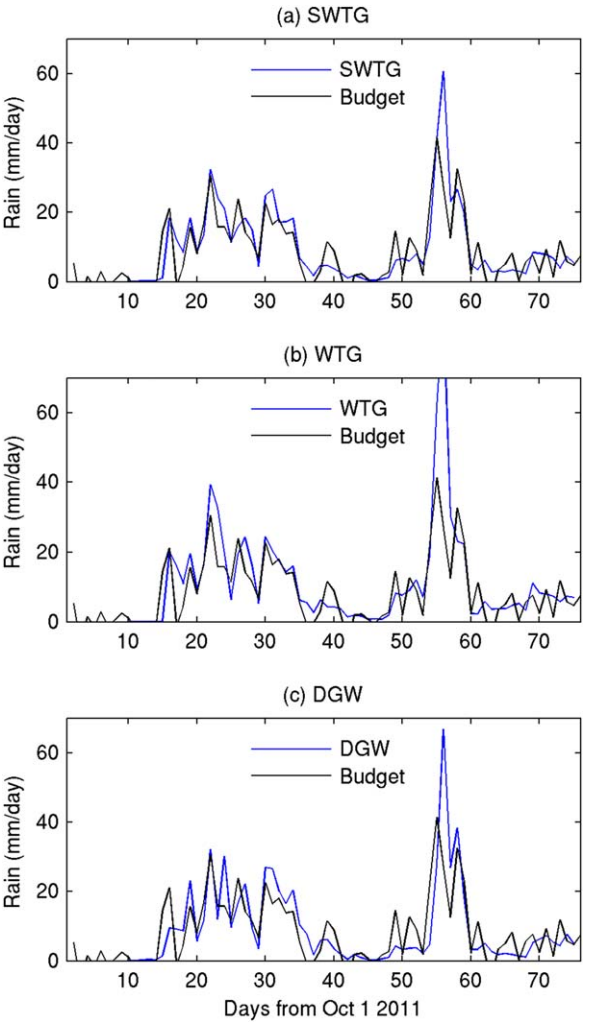

Figure 4. Time series of rain rate from simulations using the (a) SWTG, (b) WTG, and (c) DGW methods.

$$W=\sum_{n=1}^{N}\tau_1{}^{-1}\left(\frac{c_n}{c_1}\right)^{\alpha} j_n W_n. \quad (8)$$

For $\alpha=1$, each mode is weighted by the horizontal phase speed of the gravity mode. For $\alpha>0$, high wave number modes are damped as $O\left(\frac{c_n}{c_1}\right)^{\alpha}$. A few special cases may be noted: (1) for $\alpha=0$, we obtain conventional WTG; (2) for $\alpha=1$ and constant N^2, we obtain spectral WTG based on a Fourier series expansion in the vertical [*Herman and Raymond*, 2014]; (3) the $\alpha=2$ case is similar to the DGW in that high wave number W is scaled as m^2. In this study, $\tau_1=$ 1 h, $\alpha=1$, and we use the observed time mean profile for N^2.

2.2.4. Temperature Anomalies

We now discuss the target virtual temperature or potential temperature profiles used in the above equations (1), (2), and (8). In time-independent idealized simulations, θ_v^B is often taken from an RCE solution [e.g., *Sobel and Bretherton*, 2000; *Daleu et al.*, 2012]. In time-dependent problems where the aim is to simulate a specific sequence of observed weather states, however, it is not obvious what is the best option.

The target temperature profile used by *Wang et al.* [2013] was the sum of the observed temperature anomaly (defined as a departure from the time mean) and time-mean profiles obtained from a control simulation with zero large-scale vertical velocity. Figures 3a and 3b compare the observed temperature anomalies to those in the control simulation with imposed large-scale dynamics. The figure shows that the observed temperature anomalies are smaller than those in the control simulation.

Following *Edman and Romps* [2015], we use the simulated, rather than observed temperature anomalies (as well as the simulated time-mean temperature profile) to derive our target profiles for the simulations with parameterized large-scale dynamics. We find that using the temperature variations from the control run, rather than from observations, leads to improvement in the simulation of rain rates. Presumably, some combination of model bias and errors in the forcing data lead to differences in the temperature anomalies observed and those simulated with imposed large-scale dynamics; the simulated ones are inherently more consistent with the large-scale vertical motion time series which is ultimately the target of our simulations with parameterized large-scale dynamics [*Edman and Romps*, 2015].

Because of the small but finite relaxation time scale we use in the large-scale parameterizations, the model simulations with parameterized large-scale dynamics produce horizontal mean temperature anomalies very similar to, but smaller than those in the control simulation. This is shown for the SWTG run in Figure 3c.

2.2.5. Horizontal Advection of Moisture

It has been argued that horizontal moisture advection can be important to some large-scale tropical phenomena, including the MJO [e.g., *Maloney*, 2009; *Sobel et al.*, 2010; *Landu and Maloney*, 2011; *Wang and Sobel*, 2012; *Kim et al.*, 2014; *Pritchard and Bretherton*, 2014; *Zhu and Hendon*, 2015]. Horizontal advection of moisture reaches negative values of a few tens of W/m^2 in the vertical integral during the life cycles of the

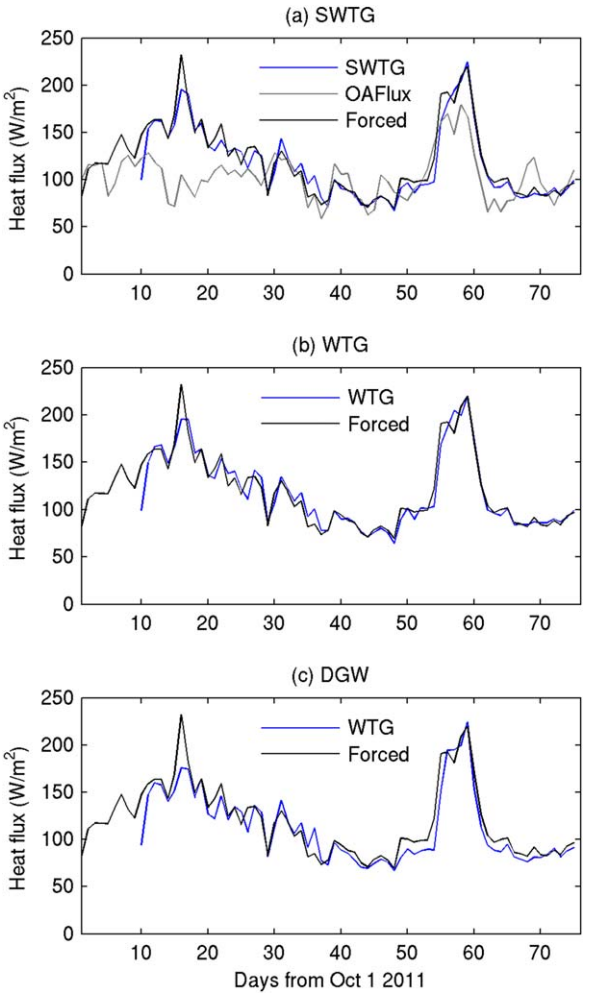

Figure 5. In blue, total surface turbulent enthalpy flux (sum of the latent and sensible heat fluxes) from (a) SWTG, (b) WTG, (c) DGW experiments. In Figure 5a, the OAFLUX observational product is shown for reference, and the result from the control simulation with imposed large-scale vertical motion is shown in all three plots (black).

DYNAMO MJO events [e.g., *Sobel et al*., 2014; *Johnson et al*., 2015], values large enough to be potentially significant to column-integrated budgets of moisture and moist static energy. Analysis of the reanalysis data set (Appendix A) indicates that the circulation associated with vorticity and divergence anomalies outside the model domain has a dominant influence on horizontal moisture advection. This suggests that it is difficult to parameterize the horizontal advection term based only on the local divergent motion (*W*). Hence, we will impose the observationally derived moisture advection Q_{hadv}, as shown in Figure 1c.

In a previous study using WTG for simulations of the MJO in the Pacific during TOGA-COARE, *Wang et al*. [2013] found that rainfall time series could reasonably reproduced without including horizontal advection of moisture. *Sobel et al*. [2014] demonstrated, however, that horizontal moisture advection is an important component of the moist static energy budget during the same two observed MJO events in the Indian Ocean during DYNAMO studied here. Here we will perform separate numerical experiments with horizontal moisture advection included or excluded to quantify its impact on the variations in surface rain rate and the vertical profile of *W*.

2.3. Numerical Model and Forcing Data

The WRF model V3.5.1 [*Skamarock et al*. 2008] is used here to perform cloud system-resolving simulations with doubly periodic lateral boundary conditions. The simulations with imposed large-scale dynamics are driven by the large-scale vertical motion and horizontal moisture advection taken from the forcing data set (version 1) derived from the DYNAMO northern sounding array observations [*Johnson and Ciesielski*, 2013; *Ciesielski et al*., 2014]. As in a number of past works [e.g., *Grabowski et al*., 1996; *Xu and Randall*, 2001; *Johnson et al*., 2002; *Tao et al*., 2004; *Khairoutdinov and Randall*, 2003; *Blossey et al*., 2007; *Varble et al*., 2011; *Fridlind et al*., 2012], large-scale vertical velocity is used to advect horizontally averaged variables (potential temperature and moisture) on the dry mass vertical coordinate, and observationally derived horizontal advective tendencies of these variables are imposed. No forcing is used for any liquid or ice hydrometeors. The lower boundary condition is daily sea surface temperature (from OAFlux as part of the NSA data set, see Fig. 1e). The domain-averaged wind profiles are relaxed to the observed values averaged over the NSA with a relaxation time of 1 h.

We use the Morrison scheme [*Morrison et al*., 2009] to parameterize microphysical transformations. This scheme predicts the mixing ratios and (for the particulate species) number concentrations of water vapor, rainwater, cloud water, cloud ice, snow, and graupel. Radiative fluxes are parameterized using the Goddard shortwave scheme [*Chou and Suarez*, 1999; *Matsui et al*., 2007; *Shi et al*., 2010] and the RRTMG longwave scheme [*Iacono et al*., 2008], respectively. The implicit damping vertical velocity scheme [*Klemp et al*., 2008] is used in the top 5 km to suppress unphysical gravity wave reflection off the top boundary. The three-dimensional Smagorinsky first-order closure scheme is applied in physical space to parameterize subgrid

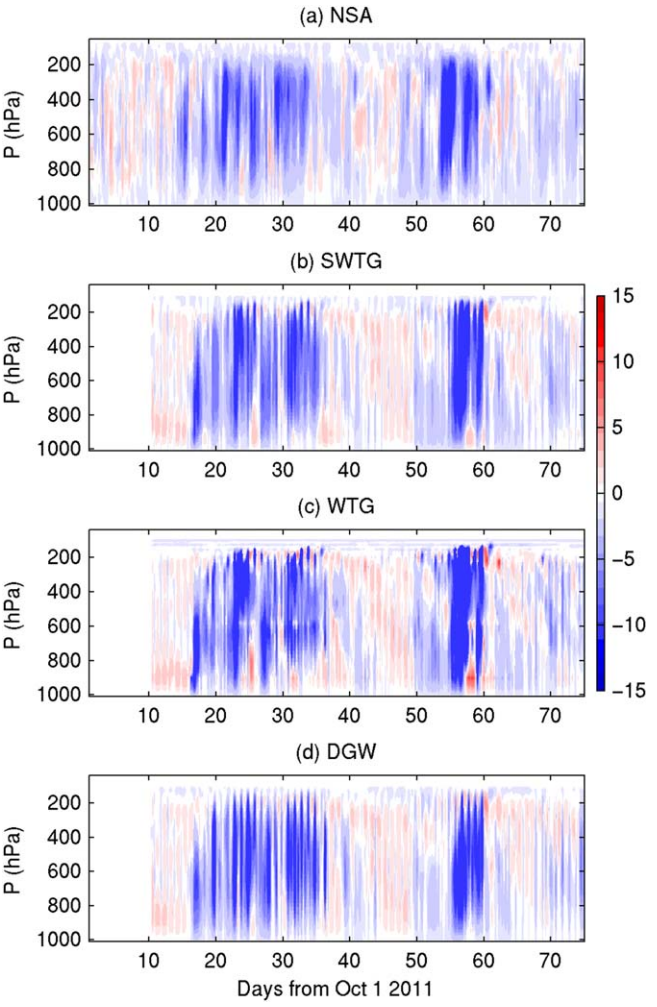

Figure 6. Large-scale pressure vertical velocity (hPa/h) from (a) the NSA observations, and simulations using (b) SWTG, (c) WTG, and (d) DGW.

scale eddies. An implicit vertical diffusion scheme similar to [*Hong et al*., 2006] is used, which ensures numerical conservation of moisture. The microphysical and turbulent mixing parameterization schemes chosen here are different from those used in our previous studies. The schemes used here were found to produce results for cloud-radiation interaction in better agreement with observations by *Wang et al*. [2015a]. The impacts of the various changes to the model made for this study are discussed in detail in Appendix B.

The dimensions of the computational domain are $64 \times 64 \times 23$ km^3, with doubly periodic lateral boundaries. The horizontal grid spacing is 1 km. A total of 60 stretched vertical levels are used with 10 levels in the first 1 km. We use a Coriolis parameter $f = 0$, since the northern sounding array is very close to the equator and the domain is small compared to the equatorial deformation radius. The solar constant at (76°E, 3°N) is uniformly specified over the domain for the calculation of shortwave radiative fluxes. The simulation with imposed large-scale forcing is very similar to those described in detail in *Wang et al*. [2015a]. The main differences between the simulations in this study and those of *Wang et al*. [2015a] is that a smaller numerical domain and different subgridscale eddy viscosity parameterization are used here, and one continuous run is used here compared to a set of shorter runs strung together in *Wang et al*. [2015a].

3. Results

3.1. Rain and Large-Scale Vertical Motion

Under the influence of strong drying by horizontal advection in the first week of DYNAMO and strong temperature anomalies in the lower levels, which effectively suppress convection [e.g., *Sessions et al*., 2015], our model simulations with interactive radiation (described in detail in section 3.2) settle into a dry state which is either permanent, or from which the simulation takes a long time to recover, and in either case in disagreement with observations. It is possible that this is in part due to the moist static energy bias in the forcing data set during that period [e.g., *Johnson et al*., 2015]. If we artificially increase the initial moisture content in these cases, the permanent or near-permanent dry state is not reached and the results are closer to observations. The sensitivity to initial moisture content, referred as "multiple equilibria," has been found in several other situations [e.g., *Sobel et al*., 2007; *Sessions et al*., 2010]. In this study, rather than imposing such an ad hoc treatment of the initial conditions, we will focus on the results from simulations initialized on 10 October, for which the problem does not occur. In the simulations with prescribed time-dependent radiation, earlier start dates can also be used without causing the spurious dry solution; however, for consistency we show runs initialized on 10 October in all cases, unless specified otherwise.

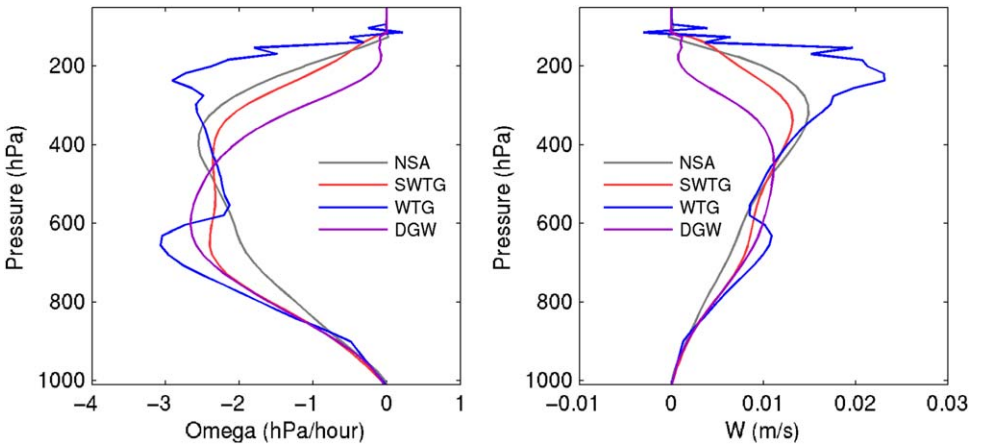

Figure 7. (left, hPa/h) Large-scale omega and (right, m/s) vertical velocity from the NSA observations, and simulations using SWTG, WTG, and DGW averaged the entire simulation period.

Precipitation time series from simulations using the three methods are shown in Figure 4. Each of these simulations used domain-averaged radiative heating taken from the forced run [*Wang et al*., 2015a], and prescribed as a function of time and height. All the methods capture the precipitation episodes associated with the two major MJO active phases and the dry conditions during early November and early December. The surface enthalpy fluxes, shown in Figure 5, all agree with the forced run, but show significant disagreement with the OAFlux product, overestimating the latter considerably during the active phases. This result differs from that in *Wang et al*. [2013] who found that surface fluxes were better captured in simulations with parameterized than imposed large-scale dynamics.

We have also repeated these runs using the observed temperature anomalies as in *Wang et al*. [2013]. Results from those experiments (Appendix B) show the two MJO episodes if horizontal moisture advection is excluded (as in *Wang et al*. [2013]), but adding horizontal moisture advection reduces the precipitation significantly compared to observations. Hence we will discuss results from the runs using target temperature from the forced run as shown in Figures 4 and 5.

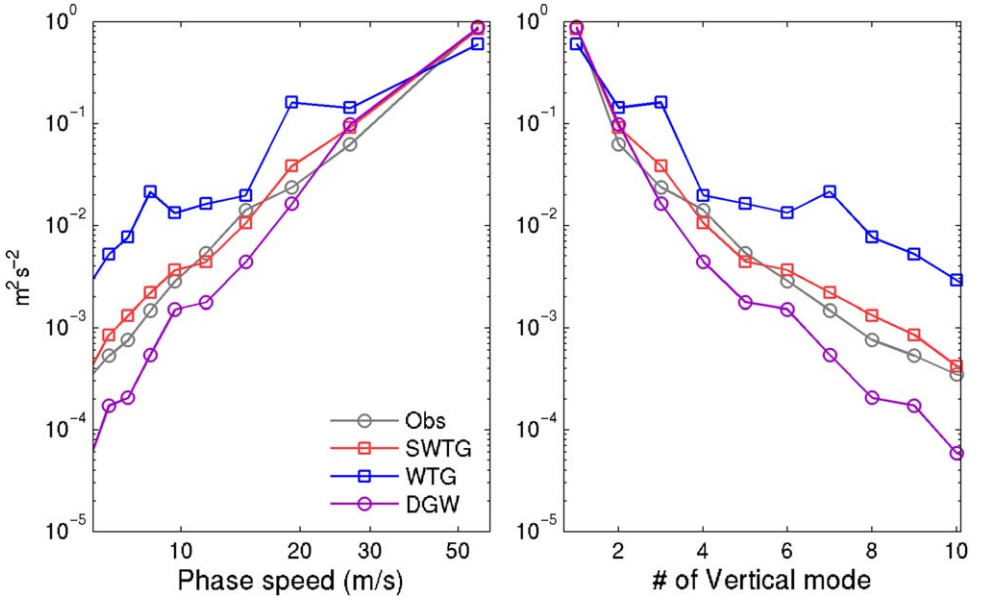

Figure 8. Vertical mode spectrum of large-scale vertical velocity *W* from NSA (observation), SWTG, WTG, and DGW, computed as the sum of projection coefficients of *W* squared, averaged over the entire simulation period and normalized by their sum.

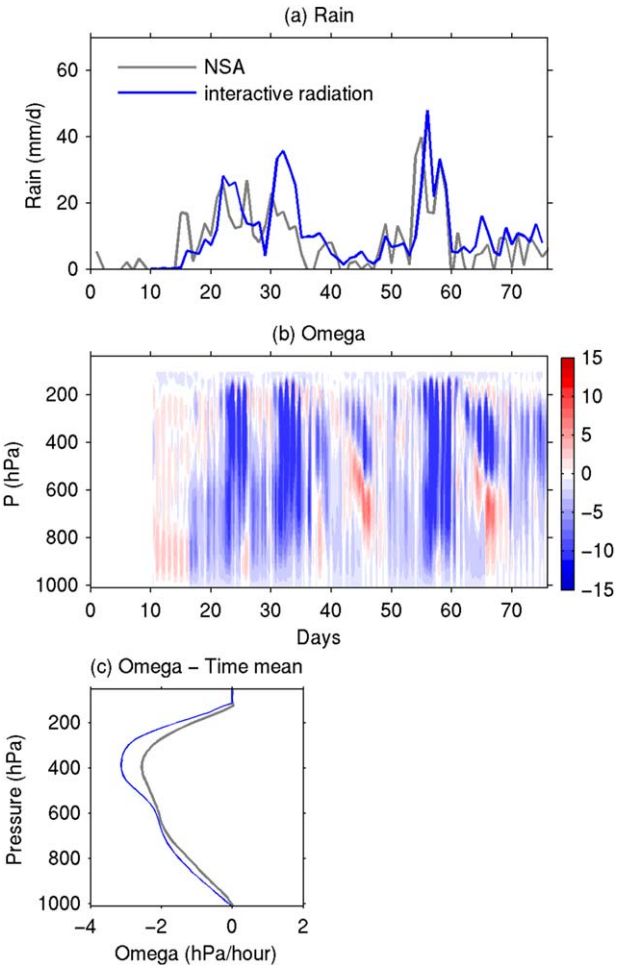

Figure 9. Results from the SWTG simulation using interactive radiation: (a) precipitation, (b) large-scale pressure vertical velocity, and (c) time-mean large-scale pressure vertical velocity (blue) compared to that derived from the sounding observations (grey).

The different methods produce significant differences in the large-scale vertical motion field despite good agreement in the rain rates. Large-scale deep ascent during the MJO active phase (Figure 6) can be seen in all the simulations, as can shallow ascent occurring before deep ascent in each MJO active phase, i.e., days 16–20, 50–55. The latter feature is less clear in the NSA data set; because the shallow ascent is relatively weak (a few hPa/h), it is possible that it is obscured by noise. The top-heavy stratiform mode [*Houze*, 1997; *Mapes*, 2000] is most conspicuous in WTG (Figure 6c) during the late stages of the MJO (e.g., day 30–35, day 55–60), but is not easy to discern in DGW or SWTG. Figure 6 also shows some high frequency oscillations in both the simulations (Figures 6b–6d) and the NSA (Figure 6a). Power spectrum analysis of omega at 500 hPa indicates that there are no statistically significant spectral peaks standing above the red-noise background. We have further tested whether the spectral slope of omega is a function of the parameters τ_1 in the SWTG simulations using additional simulations with different values of τ_1 (0.5, 1, 2, 4 h). We find that smaller τ_1 tends to make the spectrum steeper, while greater τ_1 tends to make it flatter (not shown). In the limit that τ_1 approaches infinity, the model solutions would converge to radiative-convective equilibrium, i.e., zero large-scale vertical velocity.

The time series of omega from the WTG simulation is noisier than those from the other two methods. The difference is also evident in the time-mean omega profiles (Figure 7). The time-mean sounding array-derived large-scale vertical motion is top-heavy with a peak at ~375 hPa. In contrast, WTG produces a peak at ~650 hPa, and also shows some oscillations above 300 hPa. SWTG produces a smooth profile with peaks at 350 and 650 hPa, while DGW has one peak at 600 hPa. None of these methods produces a vertical structure in perfect agreement with that derived from the sounding array. Results from WTG and DGW are largely consistent with *Wang et al.* [2013] who showed that that W from WTG was too top-heavy while that from DGW was insufficiently top-heavy. *Edman and Romps* [2015] suggest that a gravity wave resonance may produce spurious high-frequency oscillations in the prognostic DGW method. We did not find this in our DGW simulations with either prescribed radiation or interactive radiation (details below), and including the correction proposed by *Edman and Romps* [2015] has little impact on the DGW results in our case study (not shown).

Figure 8 shows the spectrum of W^2 in vertical spectral space defined above, computed as the sum of the projection coefficients of W squared. Consistent with the arguments in section 2.3, the WTG run shows excessive power at higher vertical modes, while in DGW the energy decays too quickly with wave number. Improvement in the spectrum from conventional WTG to SWTG is evident. Among the three, SWTG agrees better with W derived from the NSA observations. These results do not necessarily point to an inherent weakness of DGW, but may be a consequence of the simple constant Rayleigh damping coefficient used in our implementation of it.

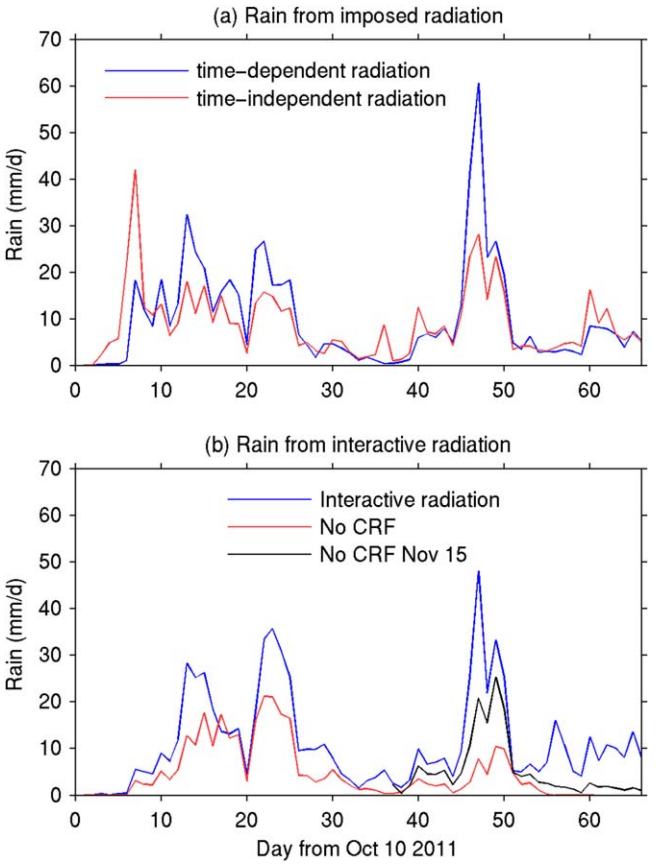

Figure 10. (a) Daily rain rates from the two simulations with (a) imposed time-dependent radiation (blue) and imposed time-independent radiation (red); (b) as (a), but with interactive radiation (blue), radiation scheme without CRF (red, cloud fields are not used in the computation of optical thickness), CRF switches off from 15 November.

3.2. Role of Radiation in Simulated MJO Dynamics

During the DYNAMO period, time variations in vertically integrated radiative heating associated with the MJO events reach 80–100 W/m^2 [*Sobel et al*., 2014]. We present additional numerical experiments to evaluate our ability to simulate these large anomalies using interactive radiation, and to assess their influence on surface precipitation in the model configurations used here.

Figure 9 shows results from a SWTG integration in which the radiation packages (RRTMG longwave and Goddard shortwave) are used to compute radiative heating interactively at each grid column, as opposed to the runs in the previous section in which time-dependent radiative heating (as a function of time and height only) taken from a run with imposed large-scale vertical motion was used. Since radiative fluxes are strongly influenced by the cloud hydrometeors from the model, this run permits cloud-radiation feedback. The variations in surface rain rate in the two MJO events as well the dry periods are all simulated with interactive radiation. This represents a significant new improvement relative to our previous work, as *Wang et al*. [2013] were unable to achieve a simulation of MJO events of this quality, or anything near it, with interactive radiation. We attribute this success to our modifications to the model itself as well as to the implementation of the large-scale dynamics parameterizations relative to those used in *Wang et al*. [2013].

On the other hand, the large-scale vertical velocity in Figure 9b shows a second baroclinic mode structure during days ~45 and ~65 in the suppressed phases. Similar behavior was found in idealized simulations with interactive radiation by *Anber et al*. [2016]. Here the presence of this structure increases the top-heaviness of the time-mean omega profile, making it closer to that derived from observations (Figure 9c). This may be fortuitous. The second mode structure appears stronger here than in the omega profile derived from observations during the same times (Figure 6a), and reducing the parameter τ_1 to 30 min, for example, would increase rain somewhat during these periods, enlarging the disagreement with observations (not shown).

To explore further the influence of radiative feedbacks, we perform additional experiments in which radiative heating is prescribed, as in Figures 4–8, but modified compared to the radiative heating fields used in those experiments.

Figure 10a shows precipitation time series from experiments in which the radiative heating profile is prescribed to be constant in time and equal to the time mean of the values used in Figures 4–8. This gives a gross measure of the impact of radiative heating anomalies associated with the MJO on the convection. The agreement between simulation and observations is significantly reduced, as the amplitude of the simulated MJO events becomes significantly smaller, and there is some indication of a phase shift as well. In both MJO events, time-independent radiation causes increased precipitation before or at the start of the active phase (e.g., the first 10 days, days 36, 40, and 60) and decreased precipitation in the peaks of the active phases by 30–50%, compared to that obtained with specified time-dependent radiation. Consistent with much previous work [e.g., *Lin and Mapes*, 2004; *Bony*

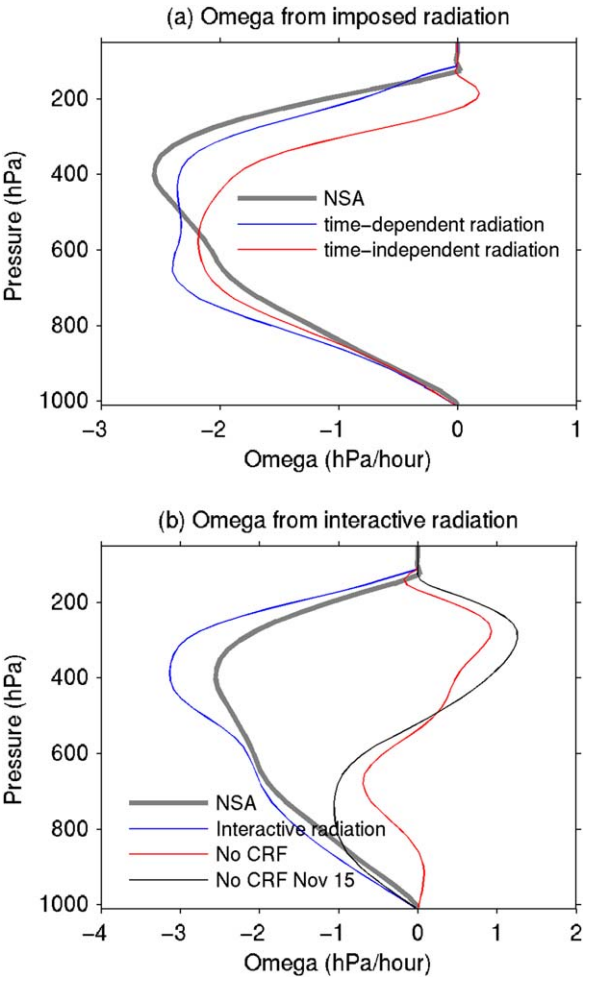

Figure 11. As Figure 9 but for time averaged pressure velocity.

and Emanuel, 2005; *Kim et al.*, 2011; *Sobel and Maloney*, 2012, 2013; *Inoue and Back*, 2015; *Creuger and Stevens*, 2015], this evidence suggests that time-dependent radiative heating anomalies associated with MJO convection are a significant source of moist static energy during the MJO active phase.

In an additional set of the SWTG experiments with interactive radiation, we compute the radiative heating using the optical thickness without cloud effects in these radiation schemes. This effectively turns off cloud-radiative feedback (CRF); a similar procedure was used to study the MJO in a global climate model by *Creuger and Stevens* [2015]. Because cloud-radiative interaction is responsible for a large fraction of the intraseasonal radiative heating anomalies—a considerably greater fraction than that due to changes in either moisture or temperature—we expect this to lead to excessive radiative cooling in the active MJO phases but to have a smaller impact during the suppressed phase when the clouds are sparse and optical thickness is small. Figure 10b shows that eliminating CRF reduces the rain rate by more than 50% during the first MJO active phase, and by 70% during the second MJO active phase. The effect of cloud-radiative feedback in the latter is overestimated because of accumulation of error over time due to the absence of CRF. This is shown by the results of another experiment, almost the same as the SWTG run with interaction radiation except that CRF is switched off starting on 15 November 2011 during the suppressed phase of the MJO. In the results from this experiment (the black curve in Figure 10b), the reduction of the precipitation during the second MJO active phase is 30–50%, similar to the effect of CRF for the October MJO active phase. In addition, this experiment also shows that the absence of CRF shuts off convection during early December, indicating the importance of CRF to the MJO suppressed phase.

The change in the time-mean omega profile is insignificant in the experiment with time-independent radiation (Figure 11a). However, the time-mean omega profile changes significantly in the experiments with no CRF, with weak large-scale descent replacing ascent in the upper troposphere. The contrast in W is associated with large difference in the time-mean column-integrated radiative heating, which is ~ -80 W/m^2 in the SWTG experiment with CRF, and ~ -150 W/m^2 without CRF. To maintain WTG (uniform temperature distribution), this excessive radiative cooling without CRF is compensated by large-scale descent induced adiabatic warming. Inspection of projection coefficients of the first 2 vertical modes indicates that switching off CRF substantially reduces the amplitude of the first mode, and changes the sign of the second mode (from top-heaviness with CRF to bottom-heaviness without CRF). Therefore, this time-mean change plays a role in the MJO changes as well; otherwise, it might be surprising that, as shown above, eliminating CRF has effects on the MJO which are as large or larger than eliminating time-dependent radiation altogether.

3.3. Effect of Horizontal Moisture Advection

The importance of the imposed horizontal moisture advection is tested by a sensitivity experiment in which we remove this forcing. Figure 12 compares the two SWTG experiments with and without horizontal moisture advection (but without interactive radiation). Without it, rain rates increase dramatically, reaching 60 mm/d during the middle of October, remain much higher than observed during the October MJO phase, and extend the

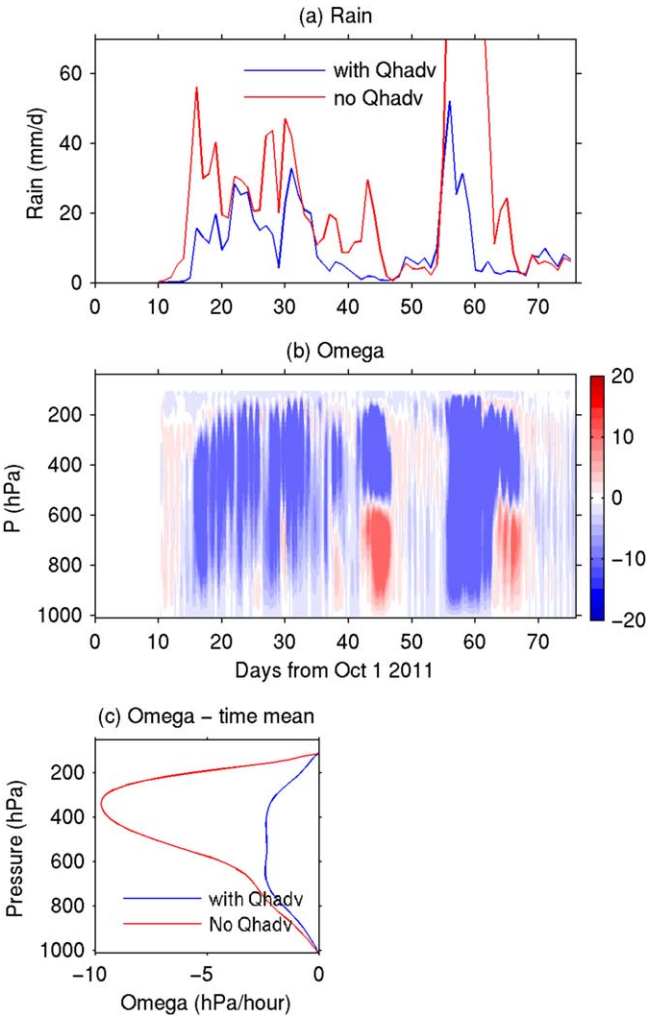

Figure 12. (a) Daily surface rain rates from the SWTG run using observed horizontal advection (blue) and without any horizontal moisture advection (red); (b) large-scale pressure vertical velocity from the SWTG run without observed horizontal advection; (c) time-mean large-scale pressure vertical velocity (red) from the same run. Note that time-mean omega from the experiment with horizontal moisture advection (blue, as in Figure 7) is also plotted for comparison.

period of high precipitation longer than in observations. An even larger overestimate is found during the November MJO active phase, even extending into the first 10 days in early December. The large-scale omega for both events (Figure 12b) shows deep ascent first, transforming gradually to excessively top-heavy profiles. Consistent with this, the time-mean omega becomes very top-heavy, with peak amplitude 3 times greater than in the experiment with horizontal moisture advection (Figure 12c). The analogous experiments using WTG or DGW show similar results (not shown). We conclude that horizontal advection of dry air plays an important role in reducing the strength of convection during and after the active phase. While the large-scale horizontal structure and propagation of the MJO are not explicitly represented in our experiments, the suppression late in the active phase is associated with eastward propagation, so our results provide further evidence that horizontal moisture advection plays a significant role in the MJO's eastward phase speed, as indicated by previous studies using other methods [e.g., *Benedict and Randall*, 2007; *Maloney*, 2009; *Sobel and Maloney*, 2012, 2013; *Andersen and Kuang*, 2012; *Pritchard and Bretherton*, 2014; *Kim et al.*, 2014; *Chikira*, 2014].

4. Conclusion

We have performed simulations of time-varying convection associated with the MJO over the Indian Ocean during the DYNAMO field campaign using a limited-domain CRM with parameterized large-scale dynamics. Three different parameterizations of large-scale dynamics were employed, including an implementation of spectral WTG (SWTG) using vertical modes derived from the vertical structure equation using the observed stratification profile. Conventional WTG and the Fourier mode-based SWTG originally presented by *Herman and Raymond* [2014] may be regarded as two special cases of this vertical mode-based SWTG method. A number of other modifications to both the WRF model and the implementation of the large-scale dynamics parameterizations were used. Time-varying radiative heating and temperature anomalies were taken from a control simulation with imposed large-scale vertical motion, rather than directly from the observations. Horizontal moisture advection, on the other hand, was taken directly from the observation-based NSA forcing data set. Additional sensitivity experiments were performed in which radiative heating and horizontal moisture advection were disabled or modified, and one in which radiative heating was computed interactively. The primary findings are as follows:

1. All three methods, with imposed time-dependent radiation and observed horizontal moisture advection, capture the variations in precipitation rate associated with the MJO with high fidelity. The large-scale vertical motion profiles from these methods differ considerably more, however: WTG produces more top-

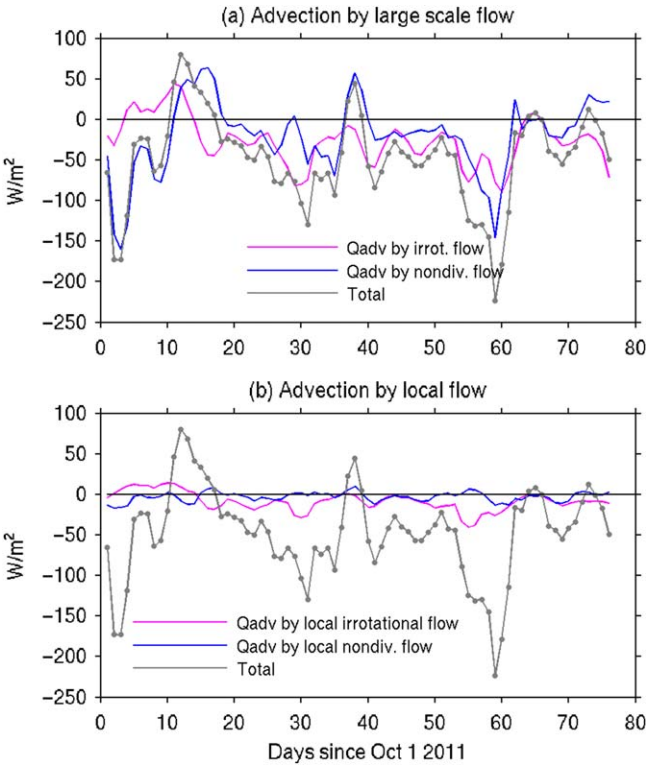

Figure A1. Column-integrated horizontal advection of moisture ($\bar{V}_h \cdot \nabla Q$, unit converted to W/m^2) over NSA (Eq—5°N, 73–80°E) derived from ERA-Interim. (top) Horizontal advection by total flow (gray), its irrational component (magenta), and nondivergent component (blue). (bottom) As in top plot except irrational and nondivergent components of the flow are computed using local divergence and vorticity averaged over NSA.

heavy and noisy omega profiles, DGW has a smooth time mean with a peak in the middle levels, and SWTG simulates a smooth profile, somewhere between those produced by WTG and DGW, in better agreement with observation. This is consistent with the relationship between W and temperature anomalies in spectral space: the latter is proportional to W scaled by the vertical wave number m as O(m^{α}), where α is 0, 1, 2 for WTG, SWTG, and DGW, respectively.

2. Simulations with interactive radiation produce agreement with observations similar to (if not quite as good as) those with imposed time-dependent radiation, as long as they are initiated on or after 10 October 2011. This is in contrast to *Wang et al.* [2013] who were not able to achieve a good simulation in broadly analogous simulations when interactive radiation was used. We attribute this success to the modifications made here both to the model and the implementation of the large-scale dynamics parameterizations.
3. Simulations with either time-independent radiative heating or with cloud-radiative feedback disabled showed significant reductions in the amplitude of the MJO precipitation anomalies.
4. In simulations without horizontal advection of moisture, the rain rates during the MJO active phases and the durations of those active phases are both greatly overestimated. The time-mean omega profile is also much top-heavier than that derived from observations.

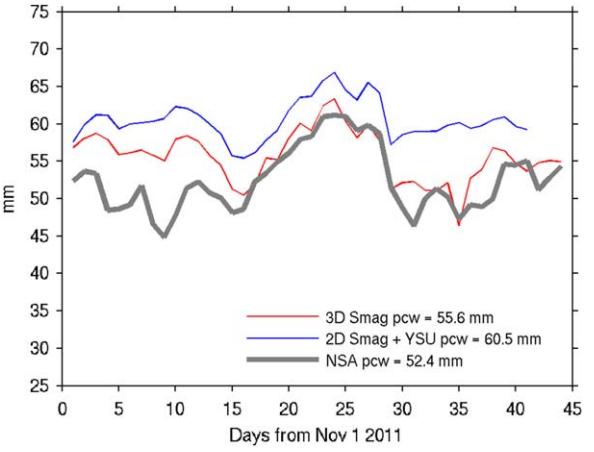

Figure A2. Time series of daily total precipitable water (PCW) from the run (blue) using turbulence scheme (YSU and 2-D Smagorinsky mixing scheme as in *Wang et al.* [2013]), the run (red) using 3-D Smagorinsky mixing scheme, and NSA (gray).

Our results highlight the importance of both horizontal advection of moisture and cloud-radiative feedbacks to the MJO. Besides implying that these processes are important to the MJO's maintenance and propagation, our results also indicate the importance of simulating these processes well in comprehensive numerical models.

Appendix A: Horizontal Advection by Large-Scale Flow

One might attempt to parameterize horizontal moisture advection in similar spirit to the parameterization of vertical advection. Two different methods have been used to parameterize horizontal moisture advection, e.g., the entrainment method [*Bergman and Sardeshmukh*, 2004; *Raymond and Zeng*, 2005;

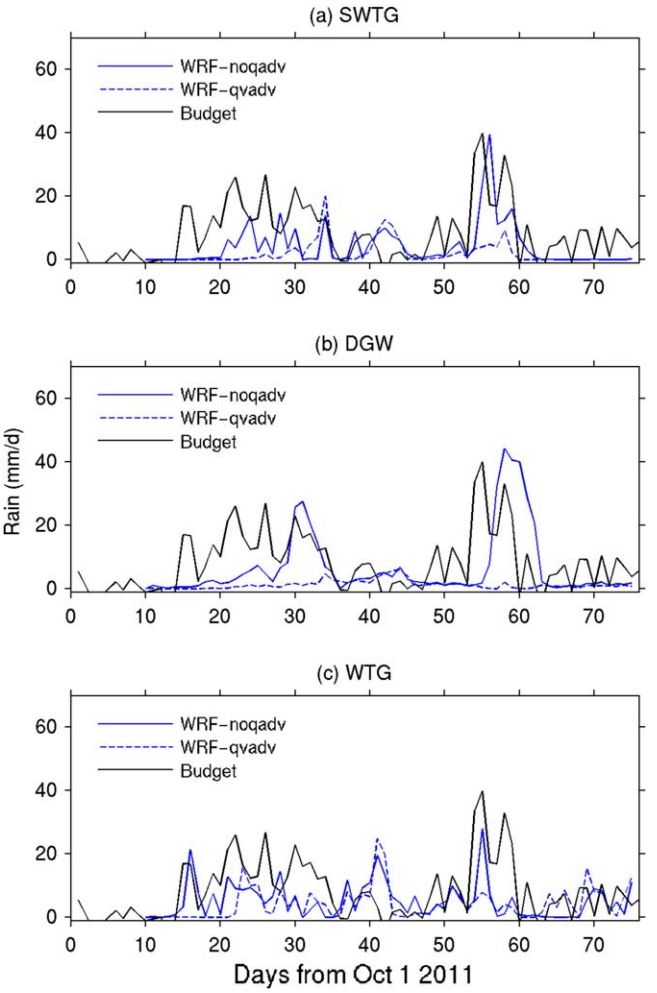

Figure A3. Surface rainfall from the runs with old model configuration as in *Wang et al.* [2013] (*Lin et al.* [1983] Microphysics and YSU [*Hong et al.* 2006] PBL PBL for turbulent eddy mixing). Target temperature is the sum of observed temperature anomalies and mean temperature profiles from zero-*W* simulation. Blue solid: without horizontal moisture advection. Dashed: with horizontal moisture advection. The parameters of these methods used for these simulations are the same as Figure 3.

Sessions et al., 2015] and the relaxation method to represent moisture advection [*Sobel and Bellon*, 2009; *Wang and Sobel*, 2012]. The primary difference between the two methods is that the former assumes that horizontal moisture advection is due to drawing of the reference profile air into the CRM domain by a divergent horizontal velocity diagnosed from the vertical WTG mass flux, while the latter assumes that remote rotational wind is of primary contribution to horizontal advection. The entrainment method has no free parameter, while the relaxation method has one free parameter—the relaxation time scale. *Sessions et al.* [2015] tested the impact of the two methods on multiple equilibria.

Here we analyze horizontal advection using the ECMWF-Interim 0.7° reanalysis data set [*Dee et al.*, 2011], which agrees reasonably with observationally derived moisture horizontal advection [*Sobel et al.*, 2014]. We argue that these methods—either based on divergent horizontal velocity or a moisture relaxation—are insufficient to represent horizontal advection of moisture in our case study of DYNAMO.

We decompose the flow as $\vec{V}=\vec{V}_\chi+\vec{V}_\psi$, where χ and ψ are scalar and vector potentials defining the irrotational and nondivergent components of the flow, and $\vec{V}_\chi$ and $\vec{V}_\psi$ are the corresponding components of the horizontal velocity. They satisfy the following relationships:

$$\begin{aligned}\Delta\chi&=\delta,\ \vec{V}_\chi=\nabla\chi,\ \text{and}\\ \Delta\psi&=\zeta,\ \vec{V}_\psi=-\vec{k}\times\nabla\psi,\end{aligned}\tag{A1}$$

where δ is divergence and ζ is vorticity. These Laplace equations are numerically solved over the entire sphere using Spherepack V3.2 [*Adams and Swarztrauber*, 1999].

Horizontal moisture advection is then computed using the moisture field combined with various flow components: the total flow, the nondivergent flow $\vec{V}_\psi\nabla q$, and the irrotational flow $\vec{V}_\chi\nabla q$. As shown in Figure A1a, moisture advection by the irrotational and vortical components are generally comparable in magnitude. Also, the sum of these two (dots) agree with the total, as they should.

We further assess the horizontal advection of moisture by the components of $\vec{V}_\chi$ and $\vec{V}_\psi$ associated directly with the divergence and vorticity in the local domain, here the NSA. This is done by setting δ and ζ outside the NSA to zero and solving equation (A1) again for $\vec{V}_\chi$ and $\vec{V}_\psi$. Figure A1b shows that horizontal advection of moisture by these local wind components contribute negligibly to the total. The lateral entrainment term for *Raymond and Zeng* [2005] can be approximately taken as $\vec{V}_\chi\nabla q$ (moisture advection by local irrotational flow, Figure A1b). Because it is small, we do not use this term in our CRM simulations. The horizontal

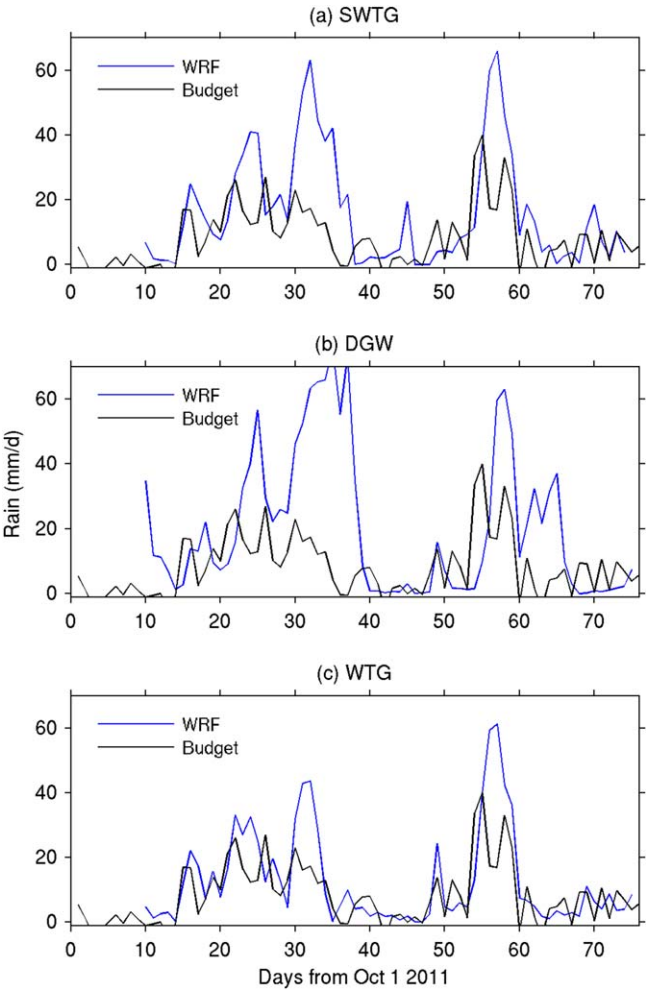

Figure A4. Surface rainfall from the runs using the old model configuration as in *Wang et al*. [2013]. Target temperature is from a simulation with imposed large-scale forcing. Blue: simulations with different methods with horizontal moisture advection. Black: budget-derived surface rainfall.

advection by the rotational wind (Figure A1a) is much larger, but we have not found that a relaxation parameterization with a single time scale [e.g., *Sobel and Bellon*, 2009] allows us to capture it well. Therefore, we apply the horizontal moisture advection directly from the observation to the CRM simulations in the present study.

Appendix B: Impact of Model Configuration

The present study differs from *Wang et al*. [2013] in that we use (1) different microphysics and turbulent mixing schemes, and (2) different target temperature profiles. The numerical model has been further tested using the DYNAMO sounding array data set. Compared with [*Wang et al*., 2013], the use of the double-moment microphysical scheme Morrison can better capture the net column-integrated radiative heating and also cloud-radiation interaction [e.g., *Wang et al*., 2015a, Figure 4c]. The use of the 3-D Smagorinsky turbulent mixing scheme reduces the excessive column-integrated water vapor. This was tested for the for the November MJO case using runs with imposed large-scale dynamics. Figure A2 shows that the use of YSU and 2-D Smagorinsky mixing scheme (as used in *Wang et al*. [2013]) overestimates PCW by ∼8 mm in the mean, while the new turbulence scheme used in this study (3-D Smagorinsky mixing scheme) substantially reduce the PCW bias. In this following, we further demonstrate the impact of these two different numerical aspects on the simulation results using parameterized large-scale dynamics.

Figure A3 shows the surface precipitation using the *Wang et al*. [2013] model. The target temperature θ_v^B is taken as the sum of observed temperature anomalies and the mean profiles of potential temperature from a zero-*W* simulation (as the imposed run but without large-scale vertical motion). The parameters are the same as the runs in Figure 4. As in *Wang et al*. [2013], these different methods (SWTG, DGW, WTG) were able to simulate the bulk MJO active phases with correlation ∼0.5 or less between the simulated and observed precipitation time series. Including horizontal moisture advection greatly degrades the simulation of precipitation (dashed curves).

Figure A4 shows results using the old configuration but with the target temperature θ_v^B taken from the imposed large-scale forcing run, rather than directly from observations. These simulations all simulate both the active and suppressed phases of the MJO events, although DGW simulates too much precipitation. Comparing Figures 3 and A4 indicates that the Morrison microphysical scheme and Smagorinsky turbulent mixing scheme have a positive impact on the simulation results with parameterized large-scale dynamics. We note that we have also performed simulations with these three methods for the TOGA-COARE case and find similar improvement.

Acknowledgments
S.W. and A.H.S. acknowledge support from the National Science Foundation under grant AGS-1062206 and the Office of Naval Research under MURI grant (N00014-12-1-0911). J.N. is supported by a Lamont Postdoctoral Fellowship. We would like to acknowledge high-performance computing support from Yellowstone (ark:/85065/d7wd3xhc) provided by NCAR's Computational and Information Systems Laboratory, sponsored by the National Science Foundation. We are grateful for the insightful and careful review by Sharon Sessions and an anonymous reviewer. Numerical simulations and the numerical model used for this research are available upon request from the corresponding author.

References

Adams, J. C., and P. N. Swarztrauber (1999), SPHEREPACK 3.0: A model development facility, *Mon. Weather Rev.*, *127*, 1872–1878.
Anber, U., S. Wang, and A. H. Sobel (2016), Response of Atmospheric Convection to Vertical Wind Shear: Cloud-System-Resolving Simulations with Parameterized Large-Scale Circulation, Part II: Effect of Interactive Radiation, *J. Atmos. Sci.*, *73*, 199–209.
Anber, U., P. Gentine, S. Wang, and A. H. Sobel (2015), Fog and rain in the Amazon, *Proc. Natl. Acad. Sci. U. S. A.*, *112*(37), 11,473–11,477, doi:10.1073/pnas.1505077112.
Andersen, J. A., and Z. Kuang (2012), Moist static energy budget of MJO-like disturbances in the atmosphere of a zonally symmetric aquaplanet, *J. Clim.*, *25*(8), 2782–2804.
Benedict, J. J., and D. A. Randall (2007), Observed characteristics of the MJO relative to maximum rainfall, *J. Atmos. Sci.*, *64*, 2332–2354.
Bergman, J., and P. D. Sardeshmukh (2004), Dynamic stabilization of atmospheric single column models, *J. Clim.*, *17*, 1004–1021.
Blossey, P. N., C. S. Bretherton, J. Cetrone, and M. Khairoutdinov (2007), Cloud-resolving model simulations of KWAJEX: Model sensitivities and comparisons with satellite and radar observations, *J. Atmos. Sci.*, *64*, 1488–1508.
Blossey, P. N., C. S. Bretherton, and M. C. Wyant (2009), Subtropical low cloud response to a warmer climate in a superparameterized climate model. Part II: Column modeling with a cloud resolving model, *J. Adv. Model. Earth Syst.*, *1*, 8, doi:10.3894/JAMES.2009.1.8.
Bony, S., and K. A. Emanuel (2005), On the role of moist processes in tropical intraseasonal variability: Cloud-radiation and moisture-convection Feedbacks, *J. Atmos. Sci.*, *62*, 2770–2789.
Ciesielski, P. E., et al. (2014), Quality-controlled upper-air sounding dataset for DYNAMO/CINDY/AMIE: Development and corrections, *J. Atmos. Oceanic Technol.*, *31*, 741–764.
Chikira, M. (2014), Eastward-propagating intraseasonal oscillation represented by Chikira-Sugiyama cumulus parameterization. Part II: Understanding moisture variation under weak temperature gradient balance, *J. Atmos. Sci.*, *71*(2), 615–639.
Chiang, J. C. H., and A. H. Sobel (2002), Tropical tropospheric temperature variations caused by ENSO and their influence on the remote tropical climate, *J. Climate*, *15*, 2616–2631.
Chou, M.-D., and M. J. Suarez (1999), A solar radiation parameterization for atmospheric studies, *NASA Tech. Rep. NASA/TM-1999-10460*, vol. *15*, 38 pp., NASA, Washington, D. C.
Creuger, T., and B. Stevens (2015), The effect of atmospheric radiative heating by clouds on the Madden-Julian Oscillation, *J. Adv. Model. Earth Syst.*, *7*, 854–864, doi:10.1002/2015MS000434.
Daleu, C. L., S. J. Woolnough, and R. S. Plant (2012), Cloud-resolving model simulations with one and two-way couplings via the weak-temperature gradient approximation, *J. Atmos. Sci.*, *69*, 3683–3699.
Daleu, C. L., et al. (2015a), Intercomparison of methods of coupling between convection and large-scale circulation. Part I: Comparison over uniform surface conditions, *J. Adv. Model. Earth Syst.*, *7*, doi:10.1002/2015MS000468.
Daleu, C. L., S. J. Woolnough, and R. S. Plant (2015b), Transition from suppressed to active convection modulated by a weak-temperature gradient derived large-scale circulation, *J. Atmos. Sci.*, *72*, 834–853.
Dee, D. P., et al. (2011), The ERA-Interim reanalysis: Configuration and performance of the data assimilation system, *Q. J. R. Meteorol. Soc.*, *137*, 553–597.
Edman, J. P., and D. M. Romps (2014), An improved weak pressure gradient scheme for single-column modeling, *J. Atmos. Sci.*, *71*(7), 2415–2429.
Edman, J. P., and D. M. Romps (2015), Self-consistency tests of large-scale-dynamics parameterizations for single-column modeling, *J. Adv. Model. Earth Syst.*, *7*, 320–334, doi:10.1002/2014MS000378.
Fridlind, A. M., et al. (2012), A comparison of TWP-ICE observational data with cloud-resolving model results, *J. Geophys. Res.*, *117*, D05204, doi:10.1029/2011JD016595.
Fulton, S. R., and W. H. Schubert (1985), Vertical normal transforms: Theory and application, *Mon. Weather Rev.*, *113*, 647–658.
Gill, A. E. (1980), Some simple solutions for heat-induced tropical circulation, *Q. J. R. Meteorol. Soc.*, *106*, 447–462, doi:10.1002/qj.49710644905.
Grabowski, W. W., X. Wu, and M. W. Moncrieff (1996), Cloud resolving modeling of tropical cloud systems during Phase III of GATE. Part I: Two-dimensional experiments, *J. Atmos. Sci.*, *53*, 3684–3709.
Herman, M. J., and D. J. Raymond (2014), WTG cloud modeling with spectral decomposition of heating, *J. Adv. Model. Earth Syst.*, *6*, 1121–1140, doi:10.1002/jame.v6.4.
Hong, S.-Y., Y. Noh, and J. Dudhia (2006), A new vertical diffusion pack- age with an explicit treatment of entrainment processes, *Mon. Weather Rev.*, *134*, 2318–2341.
Houze, R. A., Jr. (1997), Stratiform precipitation in regions of convection: A meteorological paradox?, *Bull. Am. Meteorol. Soc.*, *78*, 2179–2196.
Iacono, M. J., J. S. Delamere, E. J. Mlawer, M. W. Shephard, S. A. Clough, and W. D. Collins (2008), Radiative forcing by long-lived greenhouse gases: Calculations with the AER radiative transfer models, *J. Geophys. Res.*, *113*, D13103, doi:10.1029/2008JD009944.
Inoue, K., and L. Back (2015), Column-integrated moist static energy budget analysis on various time scales during TOGA COARE, *J. Atmos. Sci.*, *72*, 1856–1871.
Johnson, D. E., W.-K. Tao, J. Simpson, and C.-H. Sui (2002), A study of the response of deep tropical clouds to large-scale thermodynamic forcings. Part I: Modeling strategies and simulations of TOGA COARE convective systems, *J. Atmos. Sci.*, *59*, 3492–3518.
Johnson, R. H., and P. E. Ciesielski (2013), Structure and properties of Madden–Julian Oscillations deduced from DYNAMO sounding arrays, *J. Atmos. Sci.*, *70*, 3157–3179.
Johnson, R. H., P. E. Ciesielski, J. H. Ruppert, and M. Katsumata (2015), Sounding-based thermodynamic budgets for DYNAMO, *J. Atmos. Sci.*, *72*(2), 598–622, doi:10.1175/jas-d-14-0202.1.
Khairoutdinov, M., and D. A. Randall (2003), Cloud-resolving modeling of ARM Summer 1997 IOP: Model formulation, results, uncertainties and sensitivities, *J. Atmos. Sci.*, *60*, 607–625.
Kim, D., A. H. Sobel, E. D. Maloney, D. M. W. Frierson, and I.-S. Kang (2011), A systematic relationship between intraseasonal variability and mean state bias, *J. Climate*, *24*, 5506–5520.
Kim, D., J.-S. Kug, and A. H. Sobel (2014), Propagating versus nonpropagating Madden–Julian Oscillation events, *J. Clim.*, *27*, 111–125.
Klemp, J. B., J. Dudhia, and A. D. Hassiotis (2008), An upper gravity-wave absorbing layer for NWP Applications, *Mon. Weather Rev.*, *136*, 3987–4004.
Kuang, Z. (2008), Modeling the interaction between cumulus convection and linear gravity waves using a limited-domain cloud system-resolving model, *J. Atmos. Sci.*, *65*, 576–591.
Kuang, Z. (2011), The wavelength dependence of the gross moist stability and the scale selection in the instability of column integrated moist static energy, *J. Atmos. Sci.*, *68*, 61–74.
Kuang, Z. (2012), Weakly forced mock-Walker cells, *J. Atmos. Sci.*, *69*, 2759–2786.

Landu, K., and E. D. Maloney (2011), Understanding intraseasonal variability in an aquaplanet GCM, *J. Meteorol. Soc. Jpn.*, *89*, 195–210, doi:10.2151/jmsj.2011-302.
Lin, Y. L., R. D. Farley, and H. D. Orville (1983), Bulk parameterization of the snow field in a cloud model, *J. Clim. Appl. Meteorol.*, *22*, 1065–1092.
Lin, J. L., and B. E. Mapes (2004), Radiation budget of the tropical intraseasonal oscillation, *J. Atmos. Sci.*, *61*, 2050–2062.
Loeb, N. G., S. Kato, W. Su, T. Wong, F. G. Rose, D. R. Doelling, J. R. Norris, and X. Huang, (2012), Advances in understanding top-of-atmosphere radiation variability from satellite observations, *Surv. Geophys.*, *33*, 359–385, doi:10.1007/s10712-012-9175-1.
Maloney, E. D. (2009), The moist static energy budget of a composite tropical intraseasonal oscillation in a climate model, *J. Clim.*, *22*, 711–729.
Mapes, B. E. (1997), What controls large-scale variations of deep convection?, in New insights and approaches to cumulus parameterization, November 1996, pp. 157–165, ECMWF workshop proceedings, Reading, U. K.
Mapes, B. E. (2000), Convective inhibition, subgridscale triggering, and stratiform instability in a toy tropical wave model, *J. Atmos. Sci.*, *57*, 1515–1535.
Mapes, B. E. (2004), Sensitivities of cumulus ensemble rainfall in a cloud-resolving model with parameterized large-scale dynamics, *J. Atmos. Sci.*, *61*, 2308–2317.
Matsui, T., W.-K. Tao, and J. J. Shi (2007), Goddard radiation and aerosol direct effect in Goddard WRF, NASA/UMD WRF Meeting, 14 Sep., Md.
Morrison, H., G. Thompson, and V. Tatarskii (2009), Impact of cloud microphysics on the development of trailing stratiform precipitation in a simulated squall line: Comparison of one- and two-moment schemes, *Mon. Weather Rev.*, *137*, 991–1007, doi:10.1175/2008MWR2556.1.
Nie, J., and A. H. Sobel (2015), Responses of tropical deep convection to the QBO: Cloud-resolving simulations, *J. Atmos. Sci.*, *72*, 3625–3638.
Nie, J., and A. H. Sobel (2016), Modeling the interaction between quasi-geostrophic vertical motion and convection in a single column, *J. Atmos. Sci.*, doi:10.1175/JAS-D-15-0205.1, in press.
Pritchard, M., and C. S. Bretherton (2014), Causal evidence that rotational moisture advection is critical to the superparameterized Madden-Julian Oscillation, *J. Atmos. Sci.*, *71*, 800–815, doi:10.1175/JAS-D-13-0119.1.
Raymond, D. J., and S. L. Sessions (2007), Evolution of convection during tropical cyclogenesis, *Geophys. Res. Lett.*, *34*, L06811, doi:10.1029/2006GL028607.
Raymond, D. J., and X. Zeng (2005), Modelling tropical atmospheric convection in the context of the weak temperature gradient approximation, *Q. J. R. Meteorol. Soc.*, *131*, 1301–1320
Romps, D. (2012a), Numerical tests of the weak pressure gradient approximation, *J. Atmos. Sci.*, *69*, 2846–2856.
Romps, D. (2012b), Weak pressure gradient approximation and its analytical solutions, *J. Atmos. Sci.*, *69*, 2835–2845.
Sessions, S., S. Sugaya, D. J. Raymond, and A. H. Sobel (2010), Multiple equilibria in a cloud-resolving model, *J. Geophys. Res.*, *115*, D12110, doi:10.1029/2009JD013.
Sessions, S., M. J. Herman, and S. Sentic (2015), Convective response to changes in the thermodynamic environment in idealized weak temperature gradient simulations, *J. Adv. Model. Earth Syst.*, *7*, 712–738, doi:10.1002/2015MS000446.
Sentic, S., S. L. Sessions, and Z. Fuchs (2015), Diagnosing convection with weak temperature gradient simulations of DYNAMO, *J. Adv. Model. Earth Syst.*, *7*, doi:10.1002/2015MS000531.
Shi, J. J., et al. (2010), WRF simulations of the 20–22 January 2007 snow events over Eastern Canada: Comparison with in-situ and satellite observations, *J. Appl. Meteorol. Climatol.*, *49*, 2246–2266.
Skamarock, W. C., J. B. Klemp, J. Dudhia, D. O. Gill, D. M. Barker, M. G. Duda, X. Huang, W. Wang, and J. G. Powers (2008), A description of the advanced research WRF version 3, NCAR/TN-4751 STR, 125 pp., NCAR Tech. Natl. Cent. for Atmos. Res., Boulder, Colo.
Sobel, A. H., and G. Bellon (2009), The effect of imposed drying on parameterized deep convection, *J. Atmos. Sci.*, *66*, 2085–2096.
Sobel, A. H., and C. S. Bretherton (2000), Modeling tropical precipitation in a single column, *J. Clim.*, *13*, 4378–4392.
Sobel, A. H., and E. D. Maloney (2012), An idealized semi-empirical framework for modeling the Madden-Julian oscillation, *J. Atmos. Sci.*, *69*, 1691–1705.
Sobel, A. H., and E. D. Maloney (2013), Moisture modes and the eastward propagation of the MJO, *J. Atmos. Sci.*, *70*, 187–192.
Sobel, A. H., G. Bellon, and J. Bacmeister (2007), Multiple equilibria in a single-column model of the tropical atmosphere, *Geophys. Res. Lett.*, *34*, L22804, doi:10.1029/2007GL031320.
Sobel, A. H., E. D. Maloney, G. Bellon, and D. M. W. Frierson (2008), The role of surface fluxes in tropical intraseasonal oscillations, *Nat. Geosci.*, *1*, 653–657.
Sobel, A. H., E. D. Maloney, G. Bellon, and D. M. W. Frierson (2010), Surface fluxes and tropical intraseasonal variability: A reassessment, *J. Adv. Model. Earth Syst.*, *2, 2*, doi:10.3894/JAMES.2010.2.2.
Sobel, A. H., S. Wang, and D. Kim (2014), Moist static energy budget of the MJO during DYNAMO, *J. Atmos. Sci.*, *71*, 4276–4291.
Tao, W.-K., D. Johnson, C.-L. Shie, and J. Simpson (2004), The atmospheric energy budget and large-scale precipitation efficiency of convective systems during TOGA COARE, GATE, SCSMEX, and ARM: Cloud-resolving model simulations, *J. Atmos. Sci.*, *61*, 2405–2423.
Tulich, S. N., D. A. Randall, and B. E. Mapes (2007), Vertical-mode and cloud decomposition of large-scale convectively coupled gravity waves in a two-dimensional cloud-resolving model, *J. Atmos. Sci.*, *64*, 1210–1229.
Varble, A., A. M. Fridlind, E. J. Zipser, A. S. Ackerman, J.-P. Chaboureau, J. Fan, A. Hill, S. A. McFarlane, J.-P. Pinty, and B. Shipway (2011), Evaluation of cloud-resolving model intercomparison simulations using TWP-ICE observations: Precipitation and cloud structure, *J. Geophys. Res.*, *116*, D12206, doi:10.1029/2010JD015180.
Wang, S., and A. H. Sobel (2011), Response of convection to relative sea surface temperature: Cloud-resolving simulations in two and three dimensions, *J. Geophys. Res.*, *116*, D11119, doi:10.1029/2010JD015347.
Wang, S., and A. H. Sobel (2012), Impact of imposed drying on deep convection in a cloud-resolving model, *J. Geophys. Res.*, *117*, D02112, doi:10.1029/2011JD016847.
Wang, S., and A. H. Sobel (2012), Impact of imposed drying on deep convection in a cloud-resolving model, *J. Geophys. Res.*, *117*, D02112, doi:10.1029/2011JD016847.
Wang, S., A. H. Sobel, and Z. Kuang (2013), Cloud-resolving simulation of TOGA-COARE using parameterized large-scale dynamics, *J. Geophys. Res. Atmos.*, *118*, 6290–6301, doi:10.1002/jgrd.50510.
Wang, S., A. H. Sobel, A. Fridlind, Z. Feng, J. M. Comstock, P. Minnis, and M. L. Nordeen (2015a), Simulations of cloud-radiation interaction using large-scale forcing derived from the CINDY/DYNAMO northern sounding array, *J. Adv. Model. Earth Syst.*, *7*, 1472–1498, doi:10.1002/2015MS000461.
Wang, S., A. H. Sobel, F. Zhang, Y. Q. Sun, Y. Yue, and L. Zhou (2015b), Regional simulation of the October and November MJO events observed during the CINDY/DYNAMO field campaign at gray zone resolution, *J. Clim.*, *28*, 2097–2119.
Wielicki, B. A., B. R. Barkstrom, E. F. Harrison, R. B. Lee III, G. L. Smith, and J. E. Cooper, (1996), Clouds and the Earth's radiant energy system (CERES): An earth observing system experiment, *Bull. Am. Meteorol. Soc.*, *77*, 853–868, doi:10.1175/1520-0477(1996)077 < 0853:CATERE>2.0.CO;2.

Wu, Z., E. S. Sarachik, and D. S. Battisti (2000), Vertical structure of convective heating and the three-dimensional structure of the forced circulation on an equatorial beta plane. *J. Atmos. Sci.*, *57*, 2169–2187.

Xu, K.-M., and D. A. Randall (2001), Updraft and downdraft statistics of simulated tropical and midlatitude cumulus convection, *J. Atmos.Sci.*, *58*, 1630–1649.

Yoneyama, K., C. Zhang, and C. N. Long (2013), Tracking pulses of the Madden-Julian oscillation. *Bull. Am. Meteorol. Soc.*, 1871–1891, doi: 10.1175/BAMS-D-12-00157.1.

Zhu, H., and H. H. Hendon (2015), Role of large scale moisture advection for simulation of the MJO with increased entrainment, *Q. J. R. Meteorol. Soc.*, *141*, 2127–2136, doi:10.1002/qj.2510.